ADVANCED MATERIALS
www.advmat.de

Exchange Bias Between van der Waals Materials: Tilted Magnetic States and Field-Free Spin–Orbit-Torque Switching

Thow Min Jerald Cham, Reiley J. Dorrian, Xiyue S. Zhang, Avalon H. Dismukes, Daniel G. Chica, Andrew F. May, Xavier Roy, David A. Muller, Daniel C. Ralph, and Yunqiu Kelly Luo**

Magnetic van der Waals heterostructures provide a unique platform to study magnetism and spintronics device concepts in the 2D limit. Here, studies of exchange bias from the van der Waals antiferromagnet CrSBr acting on the van der Waals ferromagnet Fe_3GeTe_2 (FGT) are reported. The orientation of the exchange bias is along the in-plane easy axis of CrSBr, perpendicular to the out-of-plane anisotropy of the FGT, inducing a strongly tilted magnetic configuration in the FGT. Furthermore, the in-plane exchange bias provides sufficient symmetry breaking to allow deterministic spin–orbit torque switching of the FGT in CrSBr/FGT/Pt samples at zero applied magnetic field. A minimum thickness of the CrSBr of >10 nm is needed to provide a non-zero exchange bias at 30 K.

1. Introduction

The discovery of spin ordering persisting to the monolayer limit in vdW magnets provides a new platform for exploring magnetic phenomena that are tunable through electric gating,[1–5] optical control,[6,7] layer twisting,[8–11] and strain or pressure.[12–17] VdW magnets are easily integrated into heterostructures with other vdW materials for exploring interfacial effects and new device functionalities,[18–21] and can have magnetic structures distinct from conventional bulk magnets because the interlayer exchange is much weaker than the intralayer exchange.[22] These characteristics can be leveraged to realize non-trivial spin ordering such as coexisting antiferromagnetic and ferromagnetic order[11] or skyrmions.[23–25] Exchange-bias interactions[26] between vdW antiferromagnets (AFs) and ferromagnets (FMs) also have the potential to be particularly interesting because the interface of a layered (A-type) van der Waals antiferromagnet naturally contains only a single fully uncompensated spin sublattice, which can allow the exchange interaction at the AF/FM interface to be comparable to the interlayer interactions within each material. This produces the possibility of spatially non-uniform spin configurations not readily achievable with conventional magnetic materials. However, experiments probing exchange bias in vdW materials have thus far only considered exchange bias parallel to the anisotropy axis of the FM, visible as shifts of hysteresis curves as a function of applied magnetic field along that axis[27–32] – shifts that have been interpreted in the framework of an effectively macrospin response. Exchange interactions perpendicular to the FM's anisotropy axis in vdW heterostructures and the resulting spatially non-uniform magnetic configurations remain unexplored.

We study the interaction between ferromagnetic Fe_3GeTe_2 (FGT)[33] with perpendicular magnetic anisotropy (PMA) and antiferromagnetic CrSBr[34–36] with in-plane easy-axis anisotropy, and find that the interaction induces an *in-plane* exchange bias on the FGT. We determine an effective exchange field as strong as $B_{ext} \approx 0.15$ T at 10 K for a 9 nm FGT layer, comparable to the interlayer exchange within vdW magnets. With zero applied field and no applied current, the in-plane exchange field produces a strong tilting of the FGT magnetization. Since the exchange bias is an interface interaction and the anisotropy in FGT arises from a bulk mechanism, we conclude that the tilting is non-uniform through the thickness of FGT (illustrated schematically in **Figure 1**a). Furthermore, in CrSBr/FGT/Pt samples we observe current-driven switching of FGT without any applied magnetic field using spin–orbit torque (SOT) from the Pt layer, indicating that the in-plane exchange bias provides the necessary

T. M. J. Cham, R. J. Dorrian, X. S. Zhang, D. A. Muller, D. C. Ralph, Y. K. Luo
Cornell University
Ithaca, NY 14850, USA
E-mail: dcr14@cornell.edu; kelly.y.luo@usc.edu

A. H. Dismukes, D. G. Chica, X. Roy
Department of Chemistry
Columbia University
New York, NY 10027, USA

A. F. May
Materials Science and Technology Division
Oak Ridge National Laboratory
Oak Ridge, TN 37831, USA

D. A. Muller, D. C. Ralph, Y. K. Luo
Kavli Institute at Cornell
Ithaca, NY 14853, USA

Y. K. Luo
Department of Physics and Astronomy
University of Southern California
Los Angeles, CA 90089, USA

The ORCID identification number(s) for the author(s) of this article can be found under https://doi.org/10.1002/adma.202305739

DOI: 10.1002/adma.202305739

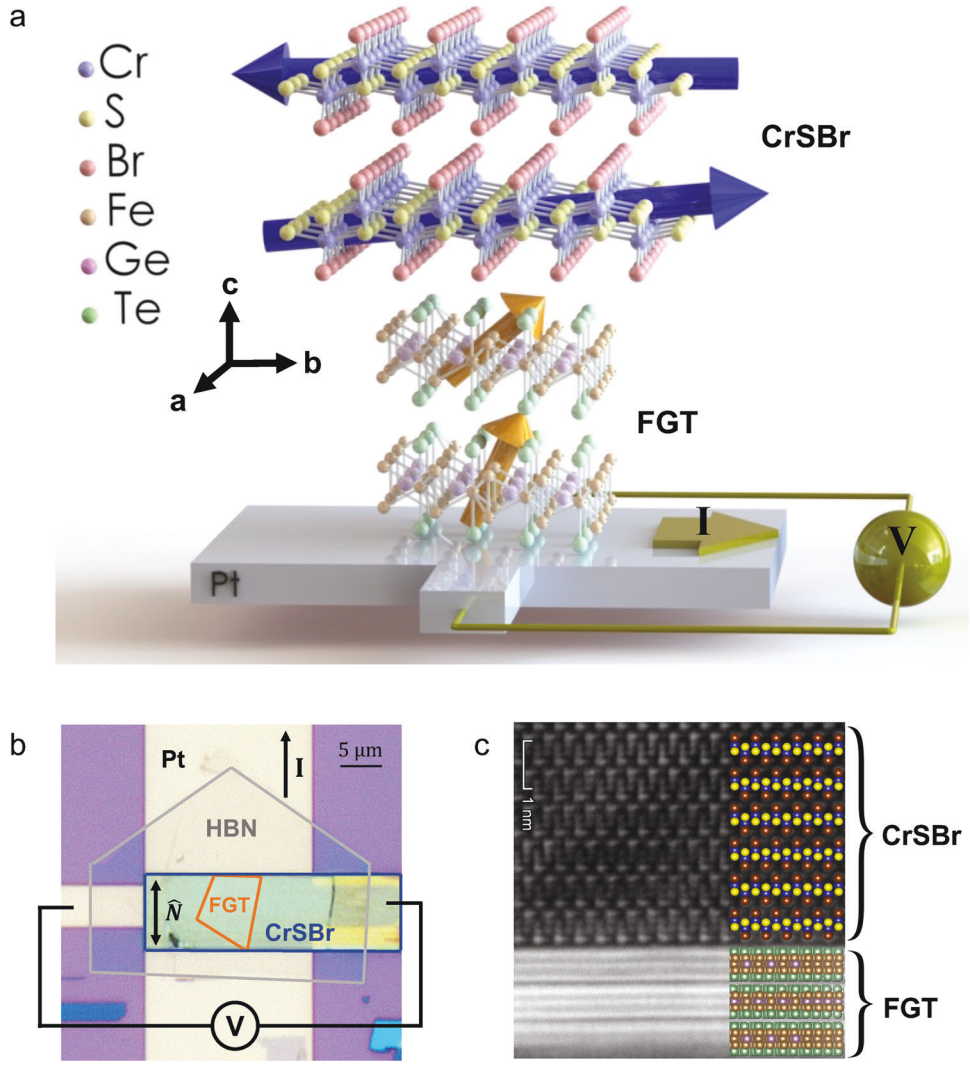

Figure 1. Device schematic and crystal structure a) Schematic of a CrSBr/FGT heterostructure dry transferred onto a Pt channel for spin–orbit torque pulse current switching measurements. The average out-of-plane magnetization of the FGT layers (orange arrows) is inferred from the Hall voltage readout transverse to the Pt channel. The magnetic moments of the CrSBr layers (blue arrows) are aligned ferromagnetically within each layer and antiferromagnetically between adjacent layers. b) Top-view optical image of the CrSBr(30 nm)/FGT(9 nm)/Pt (10 nm) device with the b crystal axis of the CrSBr layer oriented parallel to the current (so that $\hat{N} \parallel I$). c) High-angle annular dark-field (HAADF) STEM cross-sectional image of the vdW interface of a different CrSBr/FGT heterostructure. As seen from the overlaid atoms, we confirm the orientation of the *b* axis of CrSBr layer, which in this case was aligned parallel to the Pt channel.

symmetry-breaking to make the SOT switching deterministic for a magnet with PMA.

2. Results and Discussion

FGT is a metallic vdW ferromagnet with strong intra-layer and weaker interlayer ferromagnetic coupling, and a Curie temperature (T_C) of 160–190 K.[33] CrSBr is a semiconducting vdW antiferromagnet with ferromagnetic intra-layer coupling and antiferromagnetic interlayer coupling, with antiferromagnetic order below a Néel temperature (T_N) of 132 K.[34] Above this temperature, CrSBr also has an intermediate ferromagnetic phase up to ≈160 K.[35] Prior measurements on CrSBr indicate triaxial magnetic anisotropy with an in-plane easy axis along the crystallographic *b* axis (Figure 1a).[7,16,17,35–39] CrSBr flakes typically exfoliate into thin strips along the crystallographic *a* axis. This allows us to orient the Néel vector of the CrSBr flake in any desired in-plane direction. In the main text of this paper we will focus on data from two Hall-bar devices, one with the Néel vector of CrSBr parallel to the current channel of the Hall bar ($\hat{N} \parallel I$) and the other with $\hat{N} \perp I$, with layer thicknesses of CrSBr(30 nm)/FGT(9 nm)/Pt(10 nm) and CrSBr(37 nm)/FGT(12 nm)/Pt(10 nm) respectively. Figure 1b shows the sample geometry for the device with $\hat{N} \parallel I$ and Figure 1c the cross-section of the CrSBr/FGT interface in a different device.We first probe the effect of interfacial exchange coupling from CrSBr on the magnetic order of FGT using anomalous-Hall resistance measurements on CrSBr/FGT/Pt samples while sweeping an out-of-plane magnetic

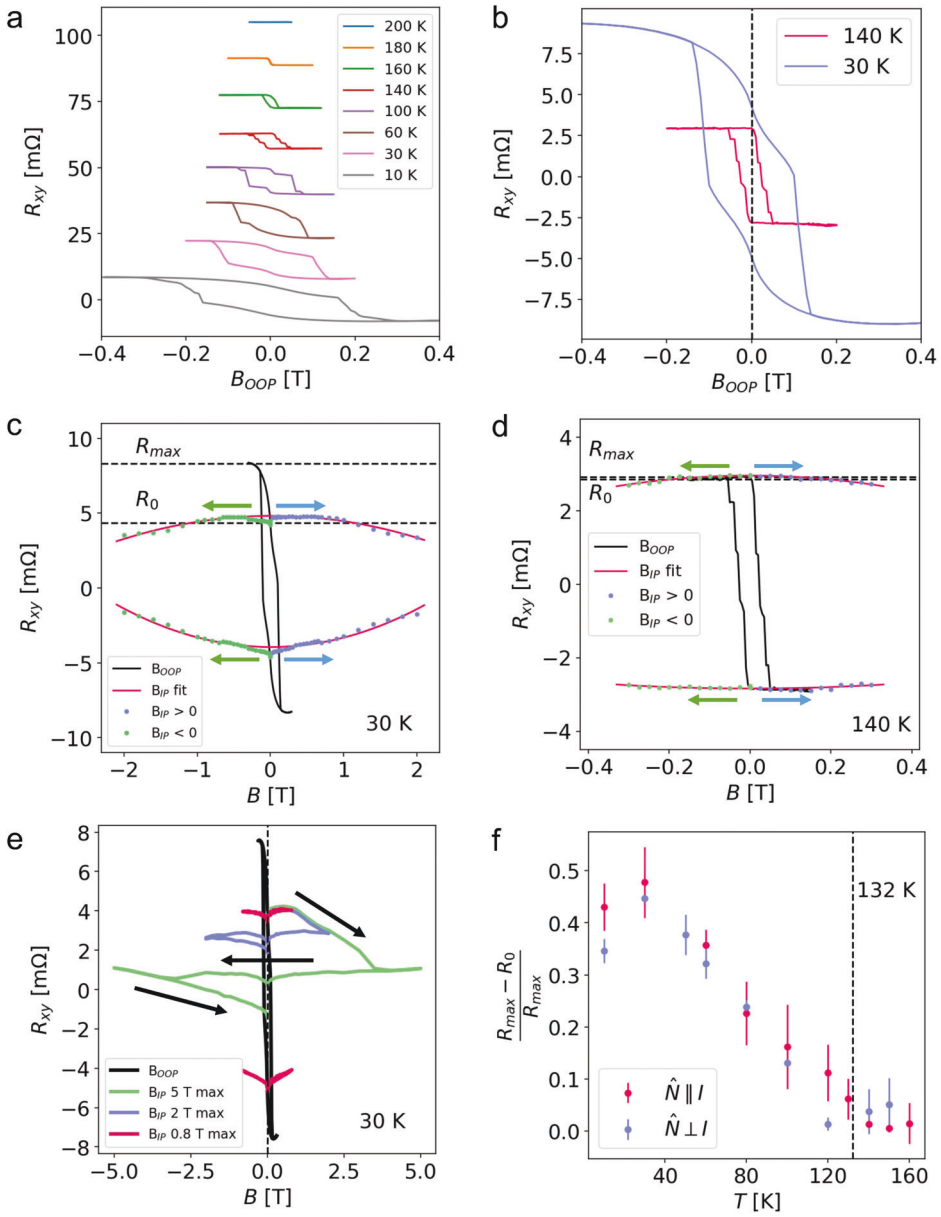

Figure 2. Anomalous Hall resistance of the CrSBr/FGT/Pt samples for out-of-plane and in-plane field sweeps. Figure 2a–e shows data from the device with $\hat{N} \parallel I$, while Figure 2f shows values from both devices ($\hat{N} \parallel I$ and $\hat{N} \perp I$). a) Anomalous Hall effect (AHE) resistance hysteresis loops as a function of applied magnetic field swept in the out-of-plane direction, for temperatures between 10 to 200 K, showing a Curie temperature for the FGT close to 180 K. Additional steps in the hysteresis loops are likely due to domain formation. b) Close-up of the AHE hysteresis loops at 30 and 140 K. A small linear component from the ordinary Hall effect was subtracted through linear fits to the data in the high field regimes, where the AHE component saturates. c,d) Anomalous Hall resistance comparing out-of-plane field sweeps to in-plane sweeps along the easy-anisotropy *b* axis of the CrSBr at (c) 30 K and (d) above the CrSBr Néel temperature at 140 K. For the in-plane field sweeps in (c) and (d), the FGT magnetization was first initialized using an out-of-plane field. The field was ramped to zero, before an in-plane field was swept either from 0 to positive (blue dots) or from 0 to negative (green dots) values. The red solid lines are parabolic fits, as guides to the eye. R_{max} indicates the Hall resistance when the FGT magnetization is fully saturated out of plane and R_0 indicates the value at zero applied magnetic field. e) Hall resistance hysteresis loops as a function of in-plane applied magnetic field swept back and forth for different maximum values of the in-plane field. f) Reduction of the Hall resistance as a function of temperature extracted from the difference between R_{max} and R_0 for the samples with $\hat{N} \parallel I$ and $\hat{N} \perp I$.

field. The much higher resistance of CrSBr relative to FGT means that the overall Hall resistance can be used as a read-out of just the FGT magnetization.[36,40] **Figure 2**a shows the out-of-plane field sweeps (10–200 K) for the sample with $\hat{N} \parallel I$ measured beginning with FGT saturated out-of-plane, showing hysteresis up to 180 K near the FGT T_C. We do not observe any horizontal shifts indicative of an out-of-plane exchange bias on the FGT for either zero-field-cooled or field-cooled samples (Section S3, Supporting Information). Notably, the hysteresis is qualitatively different above and below T_N (Figure 2b). At 140 K, the loop is close to square with

a remnant magnetization at 0 T close to the saturation value, characteristic of FGT with uniform out-of-plane magnetization.[33,40] FGT/Pt samples without CrSBr show similar close-to-square behavior from 160 to 10 K (Figure S1, Supporting Information). However, for the CrSBr/FGT/Pt sample at 30 K the hysteresis loop is far from square—there is a gradual decrease in Hall resistance as the field is swept through 0 T, indicating a reduction in the out-of-plane magnetization. If the out-of-plane field is swept from saturation to zero and then reversed (i.e., a minor loop), the Hall resistance is not hysteretic (Figure S1e,f, Supporting Information). This demonstrates that in the zero-field state the FGT magnetization has not broken up into a mix of lateral domains with positive and negative out-of-plane components, but rather the average magnetization in FGT is simply tilted away from the out-of-plane direction.

We have also studied how magnetic fields applied in the sample plane affect the magnetic configuration of the CrSBr/FGT/Pt sample with $\hat{N} \parallel I$. For the in-plane field sweeps in Figure 2c,d, we first initialize the magnetization of the FGT with an out-of-plane field just above the FGT coercivity. The field is then ramped back to zero before an in-plane field is swept in one direction, either positive or negative along the magnetic easy-axis axis of the CrSBr. We do not observe a directional exchange bias in these curves, in that a best fit indicates an average shift along the magnetic-field axis of only 0.02 ± 0.04 T at 30 K. In the discussion below we will extract an effective exchange field of 0.10–0.15 T from spin–orbit torque measurements. It is therefore sensible that an effective exchange field of this magnitude is not easily discernible in the anomalous Hall measurements versus in-plane field, as it is not far from the noise floor for that technique. Analogous experiments using 3D magnets and antiferromagnets have noted similar challenges, in that it can be difficult to detect in-plane exchange bias from the anomalous Hall resistance of magnets with perpendicular anisotropy when the effective exchange bias is weak compared to the anisotropy.[41]

Lateral domains within the FGT layer are created when the in-plane field is swept beyond about 0.8 T, as is evident from the onset of hysteresis when the in-plane field is swept back and forth without re-setting the FGT magnetization in between (Figure 2e). When the temperature is increased beyond T_N to 140 K, the maximum Hall resistance amplitude for both in-plane and out-of-plane sweeps match, as expected for a purely out-of-plane saturated magnetic state (Figure 2d). The fractional reduction in the zero-field Hall amplitude compared to the saturated value (Figure 2f) shows a very large average tilt angle away from out-of-plane for the FGT magnetization at low temperature (>50°, Figure S2k, Supporting Information). The reduction in the zero-field Hall signal reduces to zero beyond $T_N \approx 132$ K, confirming that the tilted state in the FGT is associated with the antiferromagnetism of CrSBr. We see a similar trend for the device with $\hat{N} \perp I$ (Figure 2f).

We observe that, compared to the anomalous Hall measurements, studies of spin–orbit-torque switching provide a much more sensitive means of detecting in-plane exchange bias acting on a PMA magnetic layer. In general, to achieve deterministic switching of a magnetic layer with PMA using SOT from a high-symmetry material like Pt requires an external symmetry-breaking field,[42] which can be accomplished, for example, with an applied magnetic field (B_{ext}) in the sample plane parallel to the direction of applied current,[43,44] in-plane exchange bias from an adjacent antiferromagnet or ferromagnet layer,[41,45–47] or other effective fields.[48] We perform pulsed-current measurements with different fixed B_{ext}, and after each pulse we measure the Hall voltage near zero current. Before each pulse-current switching sequence, we initialize the magnetization of the FGT with an out-of-plane field just above the coercivity. This field is then ramped back to zero, before the respective in-plane fields were applied. Figure 3a–c shows the resulting switching loops for the device with $\hat{N} \parallel I$ at 30 K. We observe deterministic switching (**Figure 3**b) for $B_{ext} = 0$ T, with the same switching chirality as when $B_{ext} = -0.1$ T (Figure 3a). When $B_{ext} = 0.1$ T, we see a quenching of the hysteresis (Figure 3c). In comparison, in the device for which $\hat{N} \perp I$, there is negligible hysteresis at 0 T (Figure 3e) and the chirality of the magnetization reversal is opposite for ±0.1 T (Figure 3d,f). When the temperature is raised above T_N to 170 K in the device with $\hat{N} \parallel I$, we see no switching at 0 T (Figure 3h) and opposite switching chiralities at ±0.05 T (Figure 3g,i). These findings indicate that a net exchange bias is induced parallel to the Néel vector of CrSBr when the temperature is lowered below T_N. This in-plane uniaxial exchange bias appears without the application of any in-plane magnetic field during the cooling process, and is unchanged in sign upon field cooling with in-plane fields up to 8 T (Section S7, Supporting Information).

We note that the switching loops show incomplete magnetization reversal. Even before the application of any current pulses, the samples begin in a state with a Hall signal less than the saturated value as described above, and then the amplitude of the current-driven hysteresis is smaller still. The existence of incomplete reversal is similar to previous reports of SOT switching of FGT/Pt heterostructures without CrSBr,[40,49,50] where this behavior was attributed to a thermally induced multidomain state at large currents.[40] We describe micromagnetic simulations that support this interpretation in Section S10 (Supporting Information).

We further investigate the current-driven magnetization switching amplitude ΔR (**Figure 4**a inset) at different values of B_{ext}. We show results for the two devices: $\hat{N} \parallel I$ and $\hat{N} \perp I$ at 170 and 30 K (Figure 4a–d). At 170 K, ΔR of both devices follow approximately an anti-symmetric Gaussian lineshape: $\Delta R = 0$ at $B_{ext} = 0$, and then $|\Delta R|$ increases as $|B_{ext}|$ increases, reaching a peak before decreasing to zero at large B_{ext} (Figure 4a,b). The switching chirality, or sign of ΔR, depends on the sign of B_{ext}, as expected for SOT mediated switching.[42] At 30 K, we see a similar anti-symmetric Gaussian field dependence for the ($\hat{N} \perp I$) device (Figure 4c), indicating the absence of exchange bias along the current direction. However, a net exchange bias is evident for the ($\hat{N} \parallel I$) device (Figure 4d), in that the overall curve is shifted along the field axis, such that $\Delta R < 0$ at $B_{ext} = 0$ and a non-zero positive B_{ext} offseting the exchange-bias is required to drive ΔR to zero. Figure 4e shows the extracted effective exchange bias (B_{EB}) from linear fits to ΔR in the low field limit as a function of temperature. For the ($\hat{N} \parallel I$) device, B_{EB} increases gradually as the temperature is lowered below about 170 K, up to ≈ 0.15 T at 10 K. However when $\hat{N} \perp I$, B_{EB} is negligible. The estimated exchange bias for the ($\hat{N} \parallel I$) device is within about a factor of two of the CrSBr interlayer exchange determined previously from antiferromagnetic resonance measurements,[39]

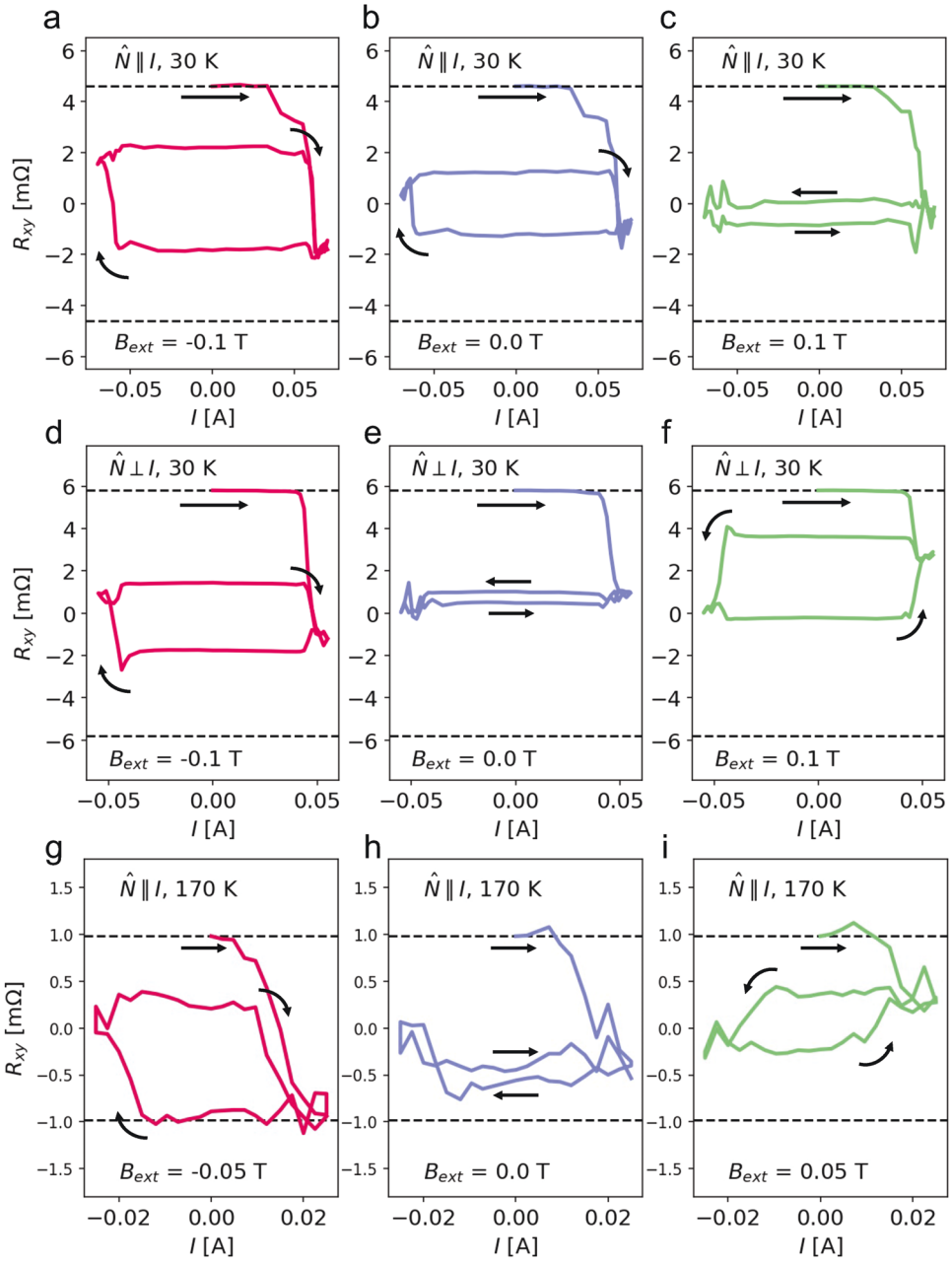

Figure 3. Pulsed-current-switching hysteresis loops of CrSBr/FGT/Pt samples. For each loop, we start the pulsed-current sequence from 0 pulsed current amplitude, go up to the maximum positive current, down to the minimum negative current, and finally back up to the maximum positive current (black arrows). a–c) Pulsed-current-switching hysteresis loops at 30 K for the sample with $\hat{N} \parallel I$. In this configuration, the uniaxial exchange bias field enables deterministic spin–orbit-torque switching within the FGT layer at 0 T (panel (b)). c) With a positive field of 0.1 T, the magnetization reversal hysteresis is quenched. d–f) Pulsed-current switching hysteresis loops at 30 K for the sample with $\hat{N} \perp I$. In contrast with the first configuration, we observe no deterministic spin–orbit-torque-driven magnetization reversal at 0 T (panel (e)). With fields of (d) −0.1 T and (f) 0.1 T, we observe hysteresis loops of opposite chiralities, as expected for a spin–orbit-torque-driven magnetization reversal process. g–i) Pulsed-current-switching hysteresis loops at 170 K, for the device with $\hat{N} \parallel I$. Unlike the behavior observed at 30 K, above the Néel temperature of CrSBr no deterministic field-free spin–orbit torque driven magnetization reversal is observed (panel (h)) and the hysteresis loops for external fields of opposite signs have opposite chiralities (panels (g,i)).

with similar temperature dependence (Section S4, Supporting Information).

Previous measurements of out-of-plane exchange bias in FGT/antiferromagnet heterostructures showed that the strength of the exchange bias depends on the antiferromagnet thickness,[27,32] with a critical thickness needed for a non-zero exchange bias effect. We performed pulsed-current hysteresis measurements to estimate the exchange bias for four different devices with $\hat{N} \parallel I$, with CrSBr thicknesses ranging from 10.5 to 47 nm, along with a Pt/FGT reference device with no CrSBr,

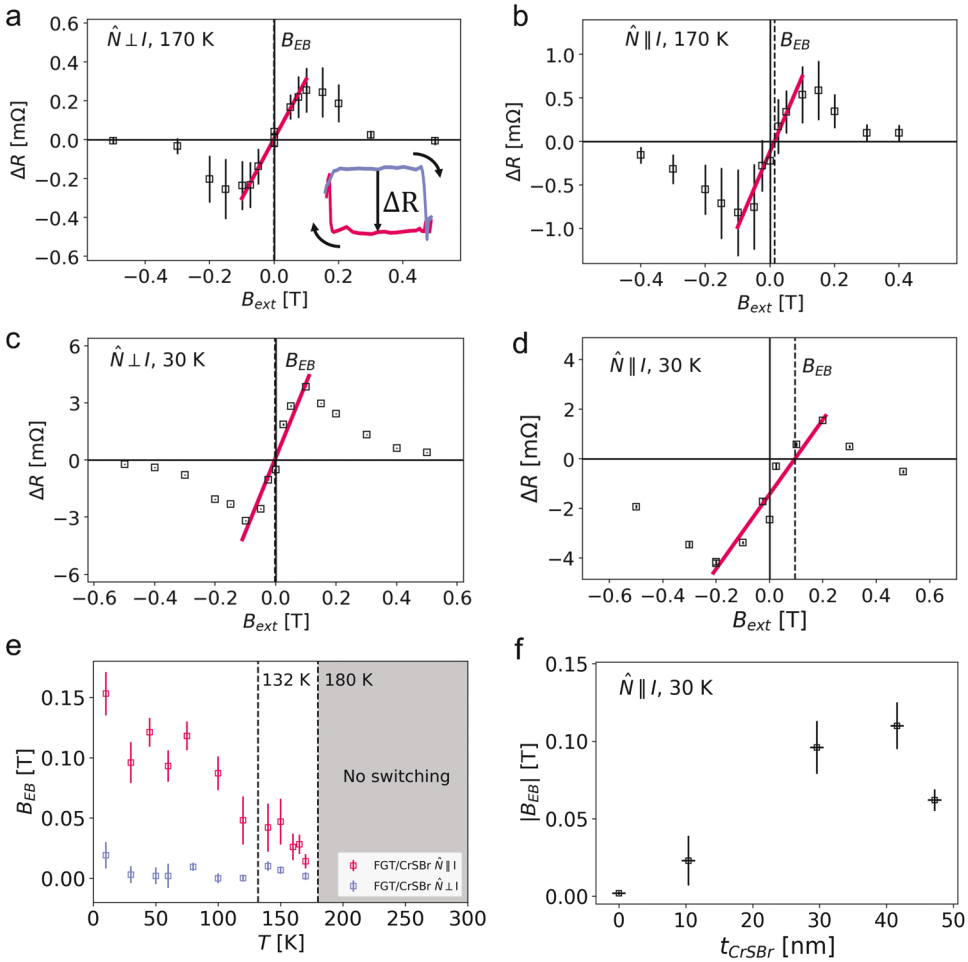

Figure 4. Magnetization reversal amplitude of CrSBr/FGT/Pt samples as a function of external fields B_{ext} applied parallel to the current axis. a–d) ΔR vs B_{ext} plots for both the $\hat{N} \parallel I$ and $\hat{N} \perp I$ devices at 30 and 170 K. We define the magnetization reversal amplitude ΔR as shown in the inset of panel (a) as the difference in Hall resistance between the state that results from spin–orbit switching at negative current (blue) and the state that results from switching at positive current (red). ΔR values are taken from the averaged difference while uncertainties are calculated from the standard deviation of R_{xy} values in the upper and lower states. At 170 K, both devices show a similar external field dependence, with $\Delta R \approx 0$ at 0 T and ΔR of opposite signs for opposite fields (panels (a) and (b)). At 30 K, while the ($\hat{N} \perp I$) device exhibits the same field dependence as the 170 K plot with $\Delta R = 0$ at $B_{ext} = 0$ T (panel (c)), the ($\hat{N} \parallel I$) device shows a distinctly different field dependence $\Delta R < 0$ at $B_{ext} = 0$ T (panel (d)). Linear fits to the low field regime are used to extract the external field strength at which the magnetization reversal is quenched (dashed lines). e) Effective exchange-bias field strength as a function of temperature for both devices. For the ($\hat{N} \parallel I$) device (red points) the exchange bias increases as T is decreased from 170 to 10 K. In contrast, the ($\hat{N} \perp I$) device does not show any significant exchange bias parallel to the current direction. f) Effective exchange-bias field strength at 30 K as a function of CrSBr thickness, indicating a critical CrSBr thickness for a non-zero B_{EB}. The four additional devices have layer thicknesses FGT(10 nm)/Pt(10 nm) with no CrSBr, CrSBr(10.5 nm)/FGT(9 nm)/Pt(10 nm), CrSBr(42 nm)/FGT(11.6 nm)/Pt(10 nm) and CrSBr(47 nm)/FGT(9.6 nm/Pt(10 nm)).

all with similar FGT thicknesses (9–12 nm). At 30 K, we see that the Pt/FGT reference sample and the thinnest ($t_{CrSBr} \approx$ 10 nm) sample show negligible B_{EB}, while the samples with t_{CrSBr} from 30 to 47 nm show non-zero exchange bias (Figure 4f; Section S6, Supporting Information). The presence of a critical CrSBr thickness for a non-zero B_{EB} further indicates that this effect arises from the exchange interaction between FGT and CrSBr.

3. Conclusion

We report measurements of an in-plane exchange bias from CrSBr acting perpendicular to the out-of-plane anisotropy of FGT, in a direction parallel to the in-plane anisotropy axis of CrSBr. This exchange field results in a strongly tilted magnetic configuration within the FGT, and can serve as an in-plane symmetry-breaking field that enables field-free deterministic switching driven by SOT in CrSBr/FGT/Pt devices. Although the CrSBr in our samples is likely in a multidomain state, we can make a rough estimate of the effective exchange bias strength from the external magnetic field required to cancel the exchange field and eliminate the deterministic switching. We estimate values as large as 0.15 T at low temperature for a 9 nm FGT layer, so that the local interaction directly at the CrSBr/FGT interface is likely an order of magnitude more. The effective exchange field decreases gradually with increasing temperature up to the

T_N of CrSBr. A CrSBr thickness greater than ≈10 nm is required to provide exchange bias for switching at 30 K. This work opens possibilities for exploiting unique characteristics of vdW magnets and heterostructures to enable new functionality in spintronics.

4. Experimental Section

CrSBr single crystals were synthesized using a modified chemical vapor transport approach originally adapted from Beck.[51] Two methods were used for the synthesis of CrSBr crystals that produced crystals of identical structure, composition, and magnetic properties. Crystals of CrSBr from Method 1 were used in all devices except for the device containing the 47 nm-thick CrSBr flake that used CrSBr crystals from Method 2. Method 1 used disulfur dibromide and chromium metal as reagents that were added together in a 7:13 molar ratio to a fused silica tube approximately 35 cm in length. This tube was sealed under vacuum and placed in a three-zone tube furnace. The tube was heated in a temperature gradient (950 to 850 °C) for 120 h. Method 2 used chromium, sulfur, and chromium tribromide as reagents in a slightly off stoichiometric ratio that were sealed in a fused silica tube of 20 cm. The tube was subjected to a modified heating profile using a two-zone tube furnace with a temperature gradient of 950 to 850 °C. Further details of the synthesis can be found in refs. [34] and [52] for Methods 1 and 2, respectively.

Bulk $Fe_{3-x}GeTe_2$ crystals were synthesized from a self-flux using an initial composition of Fe_6GeTe_9, which was homogenized above 1150 °C then cooled to 750 °C and the crystals were isolated from the flux by centrifugation. This approach yields FGT with a bulk Curie temperature above 200 K as described in refs. [53,54].

Pre-patterned Hall bars were prepared using standard photolithography processes and e-beam evaporation of 10 nm of Pt, patterned into devices with widths of 20 µm and lengths of 60 µm, with Hall leads 4 µm wide and 20 µm long. A liftoff procedure was utilized to avoid contact of the top surface of the Pt layer with photoresist. The prepared Pt bars were placed into an Ar glove box with H_2O and O_2 levels <0.5 ppm where further processing was done. First the Hall bars were heated on a hotplate at 180 °C to remove any residual adsorbed water. CrSBr and Fe_3GeTe_2 were then exfoliated onto high-resistivity silicon/silicon dioxide (280 nm) wafers using the scotch-tape method. Flakes of appropriate thicknesses were selected using an optical microscope equipped with a differential interference contrast prism for enhancing the optical contrast of steps in the flakes. The selected flakes were then mechanically transferred[55,56] using stamps made from polypropylene carbonate (PPC) and polycarbonate (PC) onto the Hall bars. The FGT flakes typically have a size of around 10 µm × 10 µm and CrSBr flakes a size of around 15 µm × 30 µm. For each device, a CrSBr flake larger than the FGT flake was used such that FGT was covered in its entirety, but the FGT flake did not extend across the entire width of the Hall bar. After completion of the transfer, polymer residue was removed in chlorofoam, and the devices rinsed in acetone and then IPA before measurements. To prevent degradation, the devices were capped with an hBN layer except the two with the thickest CrSBr layers (42 and 47 nm), and were also stored in a glovebox between measurements. We use atomic force microscopy to quantify the thicknesses and uniformity of the layers in each device. We verify that the CrSBr layers have no monolayer steps, and that the FGT layers are uniform except for some steps near the edges of the flakes.

Anomalous Hall effect and spin–orbit torque switching measurements were performed in a Quantum Design EverCool PPMS with a maximum magnetic field of 9 T. The sample was moved between the field-in-plane and field-out-of-plane configurations using a rotator. The sample was aligned on the holder such that the in-plane field was parallel to the current direction. Current pulses were applied using a Keithley 2400 sourcemeter with a pulse length of 50 µs, while the Hall voltage was measured using a Signal recovery 7265 lock-in amplifier with an output frequency of 1117.17 Hz.

Supporting Information

Supporting Information is available from the Wiley Online Library or from the author.

Acknowledgements

The authors thank Rakshit Jain, Patrick Knüppel, Steve Kriske, Liguo Ma, Aaron Windsor, and Jiacheng Zhu for experimental assistance, and inspiring discussions with Märta Tschudin, Arnab Bose, John Cenker, Vishakha Gupta, Shengwei Jiang, Kaifei Kang, Kihong Lee, Kin Fai Mak, and Jie Shan. The research at Cornell was supported by the AFOSR/MURI project 2DMagic (FA9550-19-1-0390) and the US National Science Foundation through the Cornell Center for Materials Research (DMR-1719875). T.M.J.C. was supported by the Singapore Agency for Science, Technology, and Research, and Y.K.L. acknowledges the Cornell Presidential Postdoctoral Fellowship. The work utilized the shared facilities of the Cornell Center for Materials Research and the Cornell NanoScale Facility, a member of the National Nanotechnology Coordinated Infrastructure (supported by the NSF via grant NNCI-2025233), and it benefited from instrumentation support by the Kavli Institute at Cornell. Synthesis of the CrSBr crystals was supported as part of Programmable Quantum Materials, an Energy Frontier Research Center funded by the U.S. Department of Energy (DOE), Office of Science, Basic Energy Sciences (BES), under award DE-SC0019443, and the Columbia MRSEC on Precision-Assembled Quantum Materials (PAQM) under award number DMR-2011738. FGT crystal growth and characterization (AFM) was supported by the U. S. Department of Energy, Office of Science, Basic Energy Sciences, Materials Sciences and Engineering Division. Electron microscopy was supported by the PARADIM NSF Materials Innovation Platform (DMR-2039380).

Conflict of Interest

The authors declare no conflict of interests.

Author Contributions

T.M.J.C. and Y.K.L contributed equally to this work. T.M.J.C. and Y.K.L. devised the experiment, fabricated the vdW heterostructures and performed the measurements. T.M.J.C performed the data analysis with assistance from Y.K.L. R.J.D. performed the micromagnetic simulations with assistance from T.M.J.C. and Y.K.L. X.S.Z. performed the STEM imaging, supervised by D.A.M. A.H.D. and D.G.C. synthesized the CrSBr crystals supervised by X.R. A.F.M. synthesized the FGT crystals. D.C.R. provided oversight and advice. T.M.J.C, Y.K.L., and D.C.R. wrote the manuscript. All authors discussed the results and the content of the manuscript.

Data Availability Statement

The data that support the findings of this study are available from the corresponding author upon reasonable request.

Keywords

CrSBr, exchange bias, field-free spin–orbit-torque switching, $Fe_3Ge_2Te_3$, magnetic van der Waals heterostructures, non-uniform spin configuration, uniaxial magnetocrystalline anistropy

Received: June 14, 2023
Revised: September 6, 2023
Published online: January 4, 2024

[1] W. Xing, Y. Chen, P. M. Odenthal, X. Zhang, W. Yuan, T. Su, Q. Song, T. Wang, J. Zhong, S. Jia, X. C. Xie, Y. Li, W. Han, *2D Mater.* **2017**, *4*, 024009.
[2] S. Jiang, L. Li, Z. Wang, K. F. Mak, J. Shan, *Nat. Nanotechnol.* **2018**, *13*, 549.
[3] Y. Chen, W. Xing, X. Wang, B. Shen, W. Yuan, T. Su, Y. Ma, Y. Yao, J. Zhong, Y. Yun, X. C. Xie, S. Jia, W. Han, *ACS Appl. Mater. Interfaces* **2018**, *10*, 1383.
[4] G. Zheng, W.-Q. Xie, S. Albarakati, M. Algarni, C. Tan, Y. Wang, J. Peng, J. Partridge, L. Farrar, J. Yi, Y. Xiong, M. Tian, Y.-J. Zhao, L. Wang, *Phys. Rev. Lett.* **2020**, *125*, 047202.
[5] C. Tan, W.-Q. Xie, G. Zheng, N. Aloufi, S. Albarakati, M. Algarni, J. Li, J. Partridge, D. Culcer, X. Wang, J. B. Yi, M. Tian, Y. Xiong, Y.-J. Zhao, L. Wang, *Nano Lett.* **2021**, *21*, 5599.
[6] X. Wang, C. Xiao, H. Park, J. Zhu, C. Wang, T. Taniguchi, K. Watanabe, J. Yan, D. Xiao, D. R. Gamelin, W. Yao, X. Xu, *Nature* **2022**, *604*, 468.
[7] Y. J. Bae, J. Wang, A. Scheie, J. Xu, D. G. Chica, G. M. Diederich, J. Cenker, M. E. Ziebel, Y. Bai, H. Ren, C. R. Dean, M. Delor, X. Xu, X. Roy, A. D. Kent, X. Zhu, *Nature* **2022**, *609*, 282.
[8] N. Sivadas, S. Okamoto, X. Xu, C. J. Fennie, D. Xiao, *Nano Lett.* **2018**, *18*, 7658.
[9] Q. Tong, M. Chen, W. Yao, *Phys. Rev. Appl.* **2019**, *12*, 024031.
[10] T. Song, Q.-C. Sun, E. Anderson, C. Wang, J. Qian, T. Taniguchi, K. Watanabe, M. A. McGuire, R. Stöhr, D. Xiao, T. Cao, J. Wrachtrup, X. Xu, *Science* **2021**, *374*, 1140.
[11] Y. Xu, A. Ray, Y. T. Shao, S. Jiang, K. Lee, D. Weber, J. E. Goldberger, K. Watanabe, T. Taniguchi, D. A. Muller, K. F. Mak, J. Shan, *Nat. Nanotechnol.* **2022**, *17*, 143.
[12] L. Webster, J.-A. Yan, *Phys. Rev. B* **2018**, *98*, 144411.
[13] T. Song, Z. Fei, M. Yankowitz, Z. Lin, Q. Jiang, K. Hwangbo, Q. Zhang, B. Sun, T. Taniguchi, K. Watanabe, M. A. McGuire, D. Graf, T. Cao, J.-H. Chu, D. H. Cobden, C. R. Dean, D. Xiao, X. Xu, *Nat. Mater.* **2019**, *18*, 1298.
[14] T. Li, S. Jiang, N. Sivadas, Z. Wang, Y. Xu, D. Weber, J. E. Goldberger, K. Watanabe, T. Taniguchi, C. J. Fennie, K. F. Mak, J. Shan, *Nat. Mater.* **2019**, *18*, 1303.
[15] Y. Wang, C. Wang, S.-J. Liang, Z. Ma, K. Xu, X. Liu, L. Zhang, A. S. Admasu, S.-W. Cheong, L. Wang, M. Chen, Z. Liu, B. Cheng, W. Ji, F. Miao, *Adv. Mater.* **2020**, *32*, 2004533.
[16] J. Cenker, S. Sivakumar, K. Xie, A. Miller, P. Thijssen, Z. Liu, A. Dismukes, J. Fonseca, E. Anderson, X. Zhu, X. Roy, D. Xiao, J.-H. Chu, T. Cao, X. Xu, *Nat. Nanotechnol.* **2022**, *17*, 256.
[17] G. M. Diederich, J. Cenker, Y. Ren, J. Fonseca, D. G. Chica, Y. J. Bae, X. Zhu, X. Roy, T. Cao, D. Xiao, X. Xu, *Nat. Nanotechnol.* **2023**, *18*, 23.
[18] K. L. Seyler, D. Zhong, B. Huang, X. Linpeng, N. P. Wilson, T. Taniguchi, K. Watanabe, W. Yao, D. Xiao, M. A. McGuire, K.-M. C. Fu, X. Xu, *Nano Lett.* **2018**, *18*, 3823.
[19] D. Zhong, K. L. Seyler, X. Linpeng, N. P. Wilson, T. Taniguchi, K. Watanabe, M. A. McGuire, K.-M. C. Fu, D. Xiao, W. Yao, X. Xu, *Nat. Nanotechnol.* **2020**, *15*, 187.
[20] B. Huang, M. A. McGuire, A. F. May, D. Xiao, P. Jarillo-Herrero, X. Xu, *Nat. Mater.* **2020**, *19*, 1276.
[21] J. Choi, C. Lane, J.-X. Zhu, S. A. Crooker, *Nat. Mater.* **2023**, *22*, 305.
[22] Y. Fang, S. Wu, Z.-Z. Zhu, G.-Y. Guo, *Phys. Rev. B* **2018**, *98*, 125416.
[23] B. Ding, Z. Li, G. Xu, H. Li, Z. Hou, E. Liu, X. Xi, F. Xu, Y. Yao, W. Wang, *Nano Lett.* **2019**, *20*, 868.
[24] Y. Wu, B. Francisco, Z. Chen, W. Wang, Y. Zhang, C. Wan, X. Han, H. Chi, Y. Hou, A. Lodesani, G. Yin, K. Liu, Y.-T. Cui, K. L. Wang, J. S. Moodera, *Adv. Mater.* **2022**, *34*, 2110583.
[25] B. W. Casas, Y. Li, A. Moon, Y. Xin, C. McKeever, J. Macy, A. K. Petford-Long, C. M. Phatak, E. J. Santos, E. S. Choi, L. Balicas, *Adv. Mater.* **2023**, *35*, 2212087.
[26] W. H. Meiklejohn, C. P. Bean, *Phys. Rev.* **1956**, *102*, 1413.
[27] R. Zhu, W. Zhang, W. Shen, P. K. J. Wong, Q. Wang, Q. Liang, Z. Tian, Y. Zhai, C. W. Qiu, A. T. Wee, *Nano Lett.* **2020**, *20*, 5030.
[28] L. Zhang, X. Huang, H. Dai, M. Wang, H. Cheng, L. Tong, Z. Li, X. Han, X. Wang, L. Ye, J. Han, *Adv. Mater.* **2020**, *32*, 2002032.
[29] H. Dai, H. Cheng, M. Cai, Q. Hao, Y. Xing, H. Chen, X. Chen, X. Wang, J.-B. Han, *ACS Appl. Mater. Interfaces* **2021**, *13*, 24314.
[30] Y. Wu, W. Wang, L. Pan, K. L. Wang, *Adv. Mater.* **2022**, *34*, 2105266.
[31] T. Zhang, Y. Zhang, M. Huang, B. Li, Y. Sun, Z. Qu, X. Duan, C. Jiang, S. Yang, *Adv. Sci.* **2022**, *9*, 2105483.
[32] J. Jo, F. Calavalle, B. Martín-García, D. Tezze, F. Casanova, A. Chuvilin, L. E. Hueso, M. Gobbi, *Adv. Mater.* **2022**, *34*, 2200474.
[33] C. Tan, J. Lee, S.-G. Jung, T. Park, S. Albarakati, J. Partridge, M. R. Field, D. G. McCulloch, L. Wang, C. Lee, *Nat. Commun.* **2018**, *9*, 1554.
[34] E. J. Telford, A. H. Dismukes, K. Lee, M. Cheng, A. Wieteska, A. K. Bartholomew, Y.-S. Chen, X. Xu, A. N. Pasupathy, X. Zhu, C. R. Dean, X. Roy, *Adv. Mater.* **2020**, *32*, 2003240.
[35] K. Lee, A. H. Dismukes, E. J. Telford, R. A. Wiscons, J. Wang, X. Xu, C. Nuckolls, C. R. Dean, X. Roy, X. Zhu, *Nano Lett.* **2021**, *21*, 3511.
[36] E. J. Telford, A. H. Dismukes, R. L. Dudley, R. A. Wiscons, K. Lee, D. G. Chica, M. E. Ziebel, M.-G. Han, J. Yu, S. Shabani, A. Scheie, K. Watanabe, T. Taniguchi, D. Xiao, Y. Zhu, A. N. Pasupathy, C. Nuckolls, X. Zhu, C. R. Dean, X. Roy, *Nat. Mater.* **2022**, *21*, 754.
[37] K. Yang, G. Wang, L. Liu, D. Lu, H. Wu, *Phys. Rev. B* **2021**, *104*, 144416.
[38] C. Ye, C. Wang, Q. Wu, S. Liu, J. Zhou, G. Wang, A. Soll, Z. Sofer, M. Yue, X. Liu, M. Tian, Q. Xiong, W. Ji, X. R. Wang, *ACS Nano* **2022**, *16*, 11876.
[39] T. M. J. Cham, S. Karimeddiny, A. H. Dismukes, X. Roy, D. C. Ralph, Y. K. Luo, *Nano Lett.* **2022**, *22*, 6716.
[40] X. Wang, J. Tang, X. Xia, C. He, J. Zhang, Y. Liu, C. Wan, C. Fang, C. Guo, W. Yang, Y. Guang, X. Zhang, H. Xu, J. Wei, M. Liao, X. Lu, J. Feng, X. Li, Y. Peng, H. Wei, R. Yang, D. Shi, X. Zhang, Z. Han, Z. Zhang, G. Zhang, G. Yu, X. Han, *Sci. Adv.* **2019**, *5*, eaaw8904.
[41] Y.-W. Oh, S.-H. Chris Baek, Y. Kim, H. Y. Lee, K.-D. Lee, C.-G. Yang, E.-S. Park, K.-S. Lee, K.-W. Kim, G. Go, J.-R. Jeong, B.-C. Min, H.-W. Lee, K.-J. Lee, B.-G. Park, *Nat. Nanotechnol.* **2016**, *11*, 878.
[42] L. Liu, C.-F. Pai, Y. Li, H. Tseng, D. Ralph, R. Buhrman, *Science* **2012**, *336*, 555.
[43] I. M. Miron, K. Garello, G. Gaudin, P.-J. Zermatten, M. V. Costache, S. Auffret, S. Bandiera, B. Rodmacq, A. Schuhl, P. Gambardella, *Nature* **2011**, *476*, 189.
[44] L. Liu, O. Lee, T. Gudmundsen, D. Ralph, R. Buhrman, *Phys. Rev. Lett.* **2012**, *109*, 096602.
[45] S. Fukami, C. Zhang, S. DuttaGupta, A. Kurenkov, H. Ohno, *Nat. Mater.* **2016**, *15*, 535.
[46] Y. C. Lau, D. Betto, K. Rode, J. Coey, P. Stamenov, *Nat. Nanotechnol.* **2016**, *11*, 758.
[47] A. van den Brink, G. Vermijs, A. Solignac, J. Koo, J. T. Kohlhepp, H. J. Swagten, B. Koopmans, *Nat. Commun.* **2016**, *7*, 10854.
[48] H. Wu, J. Zhang, B. Cui, S. A. Razavi, X. Che, Q. Pan, D. Wu, G. Yu, X. Han, K. L. Wang, *Mater. Futures* **2022**, *1*, 022201.
[49] M. Alghamdi, M. Lohmann, J. Li, P. R. Jothi, Q. Shao, M. Aldosary, T. Su, B. P. Fokwa, J. Shi, *Nano Lett.* **2019**, *19*, 4400.

[50] Y. Zhang, H. Xu, C. Yi, X. Wang, Y. Huang, J. Tang, J. Jiang, C. He, M. Zhao, T. Ma, J. Dong, C. Guo, J. Feng, C. Wan, H. Wei, H. Du, Y. Shi, G. Yu, G. Zhang, X. Han, *Appl. Phys. Lett.* **2021**, *118*, 262406.
[51] J. Beck, *Z. Anorg. Allg. Chem.* **1990**, *585*, 157.
[52] A. Scheie, M. Ziebel, D. G. Chica, Y. J. Bae, X. Wang, A. I. Kolesnikov, X. Zhu, X. Roy, *Adv. Sci.* **2022**, *9*, 2202467.
[53] A. F. May, J. Yan, M. A. McGuire, *J. Appl. Phys.* **2020**, *128*, 051101.
[54] G. Drachuck, Z. Salman, M. W. Masters, V. Taufour, T. N. Lamichhane, Q. Lin, W. E. Straszheim, S. L. Bud'ko, P. C. Canfield, *Phys. Rev. B* **2018**, *98*, 144434.
[55] L. Ponomarenko, A. Geim, A. Zhukov, R. Jalil, S. Morozov, K. Novoselov, I. Grigorieva, E. Hill, V. V. Cheianov, V. I. Fal'ko, K. Watanabe, T. Taniguchi, R. V. Gorbachev, *Nat. Phys.* **2011**, *7*, 958.
[56] A. K. Geim, I. V. Grigorieva, *Nature* **2013**, *499*, 419.